Vacancy formation and strain in low-temperature Cu/Cu(100) growth

Yunsic Shim[1], Valery Borovikov[1], Blas P. Uberuaga[2], Arthur F. Voter[2], and Jacques G. Amar[1]
[1]*Department of Physics & Astronomy*
University of Toledo, Toledo, Ohio 43606, USA and
[2]*Los Alamos National Laboratory, Los Alamos, New Mexico 87545, USA*
(Dated: July 2, 2008)

The development of compressive strain in metal thin films grown at low temperature has recently been revealed via X-ray diffraction and explained by the assumption that a large number of vacancies were incorporated into the growing films. The results of our molecular dynamics and parallel temperature-accelerated dynamics simulations suggest that the experimentally observed strain arises from an increased nanoscale surface roughness caused by the suppression of thermally activated events at low temperature combined with the effects of shadowing due to off-normal deposition.

PACS numbers: 81.15.Aa, 68.55.-a, 81.15.-z

Epitaxial growth has been a field of active experimental and theoretical research for the last two decades, and considerable progress has been made in understanding how deposition conditions can affect the evolving surface morphology of the growing thin film (for a recent review, see Ref. [1]). However, in many cases commercial applications require defect-free films. For this reason, understanding the processes which lead to the formation of defects under particular growth conditions is crucial if one aims to control the quality of the growing crystal.

While much of the recent work has focused on an analysis of the surface morphology, recent X-ray diffraction (XRD) experiments on low temperature Cu/Cu(100), Ag/Ag(100), and Ag(111) growth [2–4], have provided evidence for a surprisingly high vacancy concentration (2%) incorporated in the deposited thin films. In particular, as the growth temperature was decreased below 150 K, the vacancy concentration was found to increase rapidly, and then to saturate at a value somewhat above 2% for growth temperatures $T < 100$ K. In addition, after annealing to $T = 250$ K it was found that the inferred strain and vacancy concentration returns to a very low value consistent with equilibrium at this temperature.

We note that in these experiments the vacancy density was measured indirectly via the XRD pattern. In particular, the low temperature XRD profiles measured around the (100) Bragg reflection exhibited a well-pronounced asymmetry and interference fringes. The resulting diffraction patterns were then fit using a model which included as parameters the surface roughness as well as a uniform compressive strain normal to the substrate. By assuming a linear relationship between the concentration of point defects and the strain, it was estimated that a 2% vacancy concentration was present in the Cu films deposited at low temperatures. In addition, while there have been other experimental [5] and theoretical [6–8] studies of low-temperature metal growth, the surface morphology and defect structure are still not well understood. Therefore, it is of particular interest to carry out simulations to understand the nature of the transition observed in these experiments.

Here we present the results of extensive molecular dynamics (MD) and parallel temperature accelerated dynamics (parTAD) [9] simulations of Cu/Cu(100) growth carried out in order to understand the nature of the thin-film structure at low temperature. Since the interesting behavior only occurs for $T < 150$ K, while the strain and/or vacancy density saturate at even lower temperatures, here we focus primarily on simulations of growth at temperatures $T < 100$ K, using parTAD simulations at $T = 40$ K and 77 K. To understand the low-temperature limit in which thermally-activated processes become inoperative we have also carried out MD simulations.

In both the MD and parTAD simulations a Voter-Chen embedded-atom-method (EAM) potential [10] was used to describe the Cu-Cu interaction, while periodic boundary conditions were assumed parallel to the substrate (x and y directions). In addition, since three of us have recently shown [11] that the deposition angle becomes increasingly important at low growth temperature, we have carried out simulations over a range of deposition angles θ with respect to the substrate normal, ranging from 0^o (normal deposition) to 60^o [12]. To simulate the deposition process, a one-atom MD simulation was first used to describe the dynamics of the depositing atom until it was within the EAM cutoff distance σ from the growing film. As in previous work [11], the initial kinetic energy of the deposited atom corresponded to the average value $\bar{K}_i = 2k_BT_m \simeq 0.20$ eV (where T_m is the melting temperature of copper). This was then followed by a full multi-atom simulation of each impact event, in which both the depositing and surrounding substrate atoms undergo MD while several additional layers of thermostated atoms were included to dissipate the condensation energy of the depositing atom. To ensure the accuracy of our simulations of the deposition process, a variable time step was used such that the maximum atomic displacement does not exceed 0.006 $\mathring{A}$ in one integration step.

Since a single-processor (serial) simulation of every deposition event is prohibitive for the system sizes and film

thicknesses considered here, in both our parTAD and MD simulations we have implemented a parallel deposition algorithm [11] in which several atoms are deposited simultaneously in different areas of the surface. To minimize the possibility of conflicts, which may occur if the regions carved out to simulate two different deposition events overlap, we use a two-dimensional domain decomposition based on the synchronous sublattice (SL) algorithm [13]. In particular, the system is decomposed along the x and y directions into a square grid of N_p processor regions, each of which is decomposed into a 2×2 set of sublattices. At the beginning of each deposition cycle, a sublattice is randomly chosen, and each processor then selects a random initial position x_i, y_i within the chosen sublattice with height z_i equal to the long-range cutoff $r_{cut} = 7\sigma$ above the maximum height of the film [14]. We note that in kinetic Monte Carlo (KMC) simulations of growth at higher temperatures [11], this method has been shown to be accurate as long as the diffusion length of the atoms on the surface does not exceed the sublattice size. To avoid any artificial strain accumulation due to the division of the system into chunks, we also perform a global relaxation of the whole system 8 times per monolayer (ML) of atoms deposited.

Our parTAD simulations were also based on the SL algorithm [9, 13] and were carried out using square substrates with lateral dimension $L = 72$ ($N_p = 36$), in units of the bulk Cu(100) plane spacing d, and film thicknesses ranging from 7 ML for large deposition angle to 10 ML at normal incidence. In these simulations, a deposition rate $F = 5000$ ML/s was used. While this is not as slow as the experimental deposition rate of 1 ML/min, it is approximately 10^5 times slower than our MD deposition rate and hence gives a strong indication of the effects of activated events that can occur on longer time scales than MD. Accordingly, a temperature-accelerated dynamics (TAD) simulation [15] - with minimum prefactor $\nu_{min} = 10^{12}$ s^{-1}, confidence level of 90%, and high-temperature $T_{high} = 200 - 400$ K - was carried out in the appropriate sublattice by each processor over a time interval $\tau = (A_s F)^{-1}$ (where $A_s = 18$ is the number of atoms per ML in each sublattice) before moving on to the next deposition cycle. In contrast, for the less time-consuming MD simulations, system sizes ranging from $L = 72$ ($N_p = 4$) to $L = 192$ ($N_p = 16$) were used with film thicknesses up to 20 ML. We note that due to the fact that the simulation time scales approximately as N^3 (where N is the number of atoms) [9], serial TAD simulations of the system sizes and film thicknesses studied here are not currently possible. In contrast, as shown in Ref. 9, the simulation time in our parTAD algorithm scales approximately as $log(N)$. However, due to the existence of a large number of small-barrier events, the parTAD simulations for large deposition angle were significantly more time-consuming than those at normal incidence.

To investigate the effects of the long-range (LR) van der Waals attraction [16], in our MD simulations the deposition process was simulated both with and without LR attraction, while in the more time-consuming parTAD, only simulations without LR attraction ("ballistic deposition") were performed [17]. To compare with experiments [2–4] in both the parTAD and MD simulations the X-ray reflectivity as a function of the momentum transfer q_z perpendicular to the film was calculated using the expression $I(q_z) \propto \frac{1}{q_z^2} \, |\frac{N_{sub}}{1-e^{-iq_z d}} + \sum_{j=1}^{N_{film}} e^{iq_z z_j}|^2$, where N_{sub} is the number of atoms in one layer of substrate, N_{film} is the number of atoms in the deposited film, and z_j is the z-coordinate of atom j.

Fig. 1(a) shows the calculated diffraction patterns obtained from our parTAD (MD) simulations up to 10 ML (20 ML) at normal incidence ($\theta = 0^o$). As can be seen, there is relatively little asymmetry in the diffraction pattern up to 20 ML and only minimal reflectance oscillations, as well as good agreement between the parTAD and MD results. Similar results (not shown) have also been obtained for $\theta = 30^o$. In contrast, in our simulations at higher deposition angles ($\theta = 55^o - 60^o$) strong reflectance oscillations can be seen, as shown in Figs. 1(b) - (d). In particular, as shown in Fig. 1(b) there is good qualitative agreement between the calculated XRD pattern obtained from our MD simulations for $\theta = 55^o$ and the experimentally determined diffraction pattern at $T = 110$ K [3]. In addition, as shown in Fig. 1(c), for a deposition angle of 60^o, interference peaks can already be seen in our 77 K parTAD simulations at 6 ML. A comparison of our parTAD and MD results also indicates that the effect of activated events is to soften the interference peaks. Thus, our XRD simulation results confirm our assumption [18] about the off-normal deposition conditions in the experiments of Refs. 2–4.

We now consider the origin of the reflectance oscillations observed in our simulations. As suggested in Refs. 2–4, one of the major causes is interference effects due to compressive strain in the deposited film. This is confirmed by the simulation results of Fig. 2(a) which shows the average compressive strain ε_c in the z-direction, averaged over 20 ML of film-plus-substrate. Here $\varepsilon_c = (d - d_{film})/d$ where d_{film} is the average height difference between an atom and its nearest-neighbor atoms in the plane below. For large deposition angles and coverages larger than 5 ML there is significant strain, while for smaller deposition angles the average strain increases much less rapidly with increasing coverage.

What is the cause of the compressive strain? In Refs. 3 and 4 it was suggested that the strain was primarily due to vacancies. However, as shown in Fig. 2(b) due to the existence of a significant number of deposition-induced events in our simulations, the vacancy density in the growing film is an order of magnitude smaller than the inferred experimental value of 2%. This is in contrast to KMC simulations with restricted downward funneling

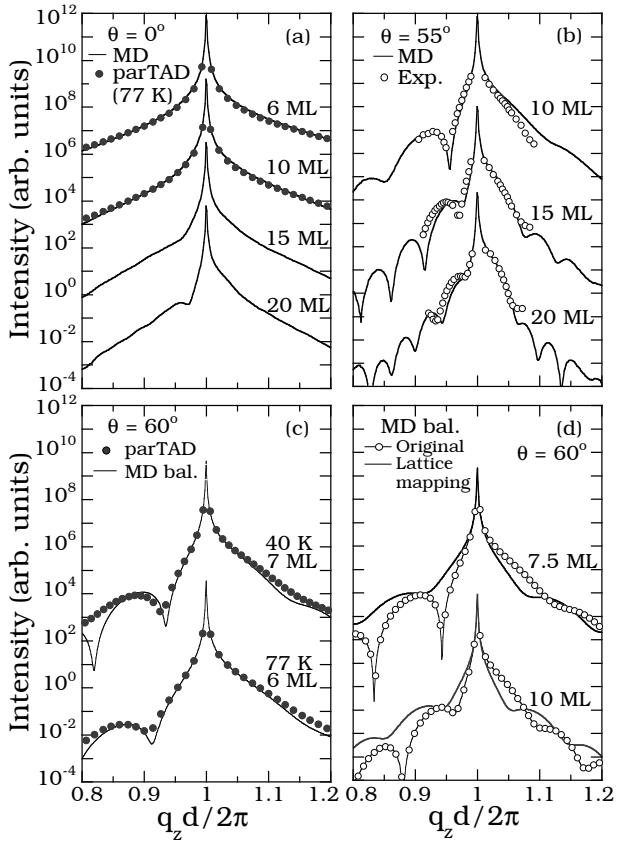

FIG. 1: Evolution of reflectivity line shape as a function of deposition angle and coverage. MD results in (a)-(b) correspond to LR attraction while all other results correspond to ballistic deposition. Experimental results in (b) are from Ref. [2].

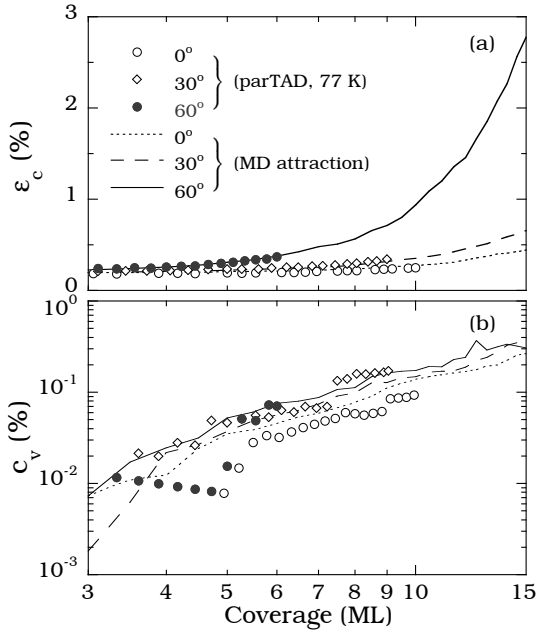

FIG. 2: (a) Average compressive strain ε_c and (b) vacancy density c_v in growing film as a function of deposition angle and coverage.

[8] in which vacancy defect densities of $15\% - 30\%$ were obtained. In addition, the vacancy density is only weakly dependent on the deposition angle and so cannot explain the strong dependence of the XRD pattern on deposition angle. As a test, we have filled in the vacancies in our simulated films and then relaxed the configurations. In all cases, there was no significant change in either the average compressive strain or the calculated XRD pattern. Thus, while some vacancy formation does occur in our simulations, it is not the cause of the compressive strain or the experimentally observed reflectance oscillations.

To understand the origin of the compressive strain for large deposition angles we consider the surface morphologies obtained in our simulations. As can be seen in Figs. 3 and 4(a), while the surface roughness remains relatively small for $\theta \leq 30^o$, for larger deposition angles ($\theta = 60^o$) the surface roughness and density of surface atoms increase rapidly with increasing coverage. In addition, for large deposition angles the effects of shadowing, which prevents 'valleys' from filling in, combined with the suppression of thermally activated processes such as downward funneling (DF) [19], leads to small-scale protruding structures as shown in Fig. 3(c). The formation of such "nanostructures" strongly enhances the surface atom density, while the relaxation of the corresponding surface atoms [20], leads to the large compressive strain. An analysis of the evolution of our XRD patterns also indicates that the onset of oscillations corresponds to the formation of vertical (100) cliffs in the film, as shown in Fig. 3(d). In this connection, we note that KMC simulations with downward funneling but no other activated events can lead to a rough surface with nanoscale pyramidal structures for large deposition angles. However, they do not lead to overhangs or significant compressive strain nor does the corresponding XRD pattern exhibit significant interference oscillations.

In order to further understand the effects of deposition angle on the surface morphology we have also measured the density ρ_m of atoms with missing four-fold-hollow support sites or "overhangs". As shown in Fig. 4(b), ρ_m is significantly higher for a large deposition angle ($\theta = 60^o$) than at smaller deposition angles. In addition, due to the existence of activated events, the surface roughness and density of missing support sites in our 77 K parTAD simulations is somewhat lower than in the MD simulations. We also note that - as shown by the solid curves in Fig. 1(d), which correspond to XRD patterns calculated by first "mapping" all atoms to the nearest fcc lattice site - the presence of a rough surface with overhangs can lead to reflectance oscillations, even without strain relaxation. However, the accompanying strain significantly enhances the diffraction oscillations for $q_z d/2\pi < 1$ and shifts them to larger q_z. Thus, our results indicate that the observed diffraction oscillations

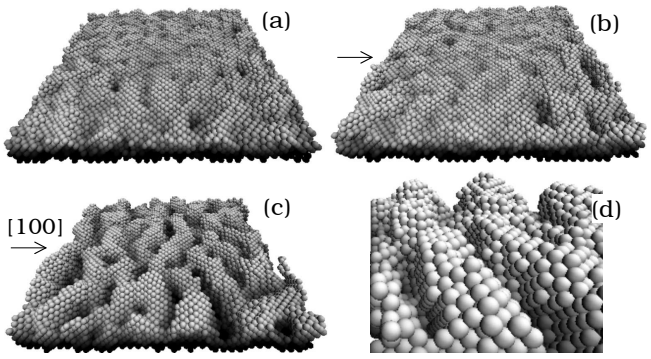

FIG. 3: Surface morphology for 7 ML parTAD films at $T = 40$ K ($L = 72$) for case of (a) normal incidence (b) $\theta = 30^o$ and (c) $\theta = 60^o$. (d) shows blow-up of portion of (c). Arrows in (b) - (c) indicate azimuthal orientation of deposition.

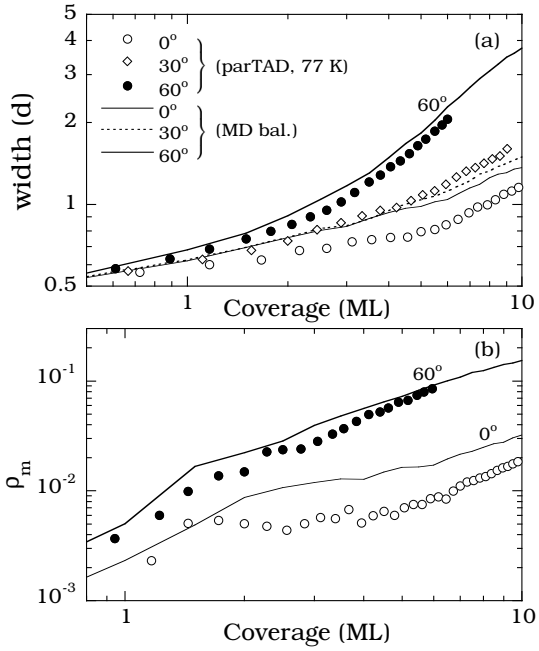

FIG. 4: (a) Surface roughness and (b) density of missing support sites ρ_m as a function of deposition angle and coverage.

are due to the existence of a rough surface with overhangs combined with the resulting compressive strain.

It is also interesting to consider the temperature dependence in our parTAD simulations. As expected, the number of activated events at 77 K was significantly larger than at 40 K, and excluding repetitive small-barrier events, was approximately equal to the number of deposition-induced events (approximately 0.1 per deposited particle). A comparison of the surface morphology at 6 ML and $\theta = 60^o$ (not shown) also indicates that the resulting 'ripples' tend to be somewhat longer and more well aligned at 77 K than at 40 K. We note that the maximum barrier for accepted events at 77 K (0.13 eV) was twice as large as that at 40 K, while an analysis of the energy barriers for rejected DF events leads to a distribution with a sharp peak at 0.33 eV and a maximum at 0.42 eV. Taking into account the difference between the parTAD and experimental deposition rates and extrapolating to a temperature at which these high-barrier rejected DF events would just begin to become active leads to a predicted transition temperature $T_c \simeq 120 - 150$ K in good agreement with experiment.

In conclusion, our simulation results suggest that the key factor responsible for the experimentally observed strain accumulation in the films grown at low temperature is an increased nanoscale surface roughness due to the suppression of thermally activated events combined with the effects of shadowing due to off-normal deposition conditions. The resulting surface roughness leads to a surface morphology with (100) cliffs and protrusions in the film. Our results also indicate that while some vacancy formation occurs at low temperature, the resulting vacancy density is significantly smaller than the inferred experimental value, and is not necessary to explain the large compressive strain.

The authors gratefully acknowledge fruitful discussions with Paul Miceli. This work was supported by NSF grant DMR-0606307 as well as by grants of computer time from the Ohio Supercomputer Center and NCSA. Work at Los Alamos National Laboratory (LANL) was supported by the DOE Office of Basic Energy Sciences and by the LDRD program. LANL is operated by Los Alamos National Security, LLC, for the National Nuclear Security Administration of the U.S. DOE under Contract No. DE-AC52-06NA25396.

[1] J.W. Evans, P.A. Thiel, and M.C. Bartelt, Surf. Sci. Rep. **61**, 1 (2006).
[2] C. E. Botez, W.C. Elliott, P.F. Miceli, and P.W. Stephens, Phys. Rev. B **66**, 075418 (2002).
[3] C. E. Botez, P.F. Miceli, and P.W. Stephens, Phys. Rev. B **66**, 195413 (2002).
[4] C. E. Botez, K. Li, E. D. Lu, W. C. Elliott, P. F. Miceli, E. H. Conrad, and P.W. Stephens, Appl. Phys. Lett. **81**, 4718 (2002).
[5] C. R. Stoldt, K. J. Caspersen, M. C. Bartelt, C. J. Jenks, J. W. Evans, and P. A. Thiel, Phys. Rev. Lett. **85**, 800 (2000).
[6] L. Dong, R.W. Smith, and D.J. Srolovitz, J. Appl. Phys. **80**, 5682 (1996).
[7] F. Montalenti and A.F. Voter, Phys. Rev. B **64**, 081401(R) (2001); F. Montalenti, M.R. Sørensen, and A.F. Voter, Phys. Rev. Lett. **87**, 126101 (2001).
[8] K.J. Caspersen and J.W. Evans, Phys. Rev. B **64**, 075401 (2001).
[9] Y. Shim, J.G. Amar, B.P. Uberuaga, and A.F. Voter, Phys. Rev. B **76**, 205439 (2007).
[10] A. F. Voter, Phys. Rev. B **57**, R13985 (1998).
[11] V. Borovikov, Y. Shim, and J.G. Amar, Phys. Rev. B **76**, 241401(R) (2007).

[12] The results presented here correspond to an azimuthal angle such that the [100] direction lies in the plane of incidence (see Fig. 3). However, for comparison we have also carried out some simulations with the azimuthal angle rotated by 45^o, and very little difference was found.
[13] Y. Shim and J.G. Amar, Phys. Rev. B **71**, 125432 (2005).
[14] In case of conflict, the depositions are carried out sequentially rather than simultaneously.
[15] M. R. Sørensen and A. F. Voter, J. Chem. Phys. **112**, 9599 (2000).
[16] J.G. Amar, Phys. Rev. B **67**, 165425 (2003).
[17] For the angles of interest ($\theta \simeq 55^o - 60^o$), the main effect of LR attraction is to slightly reduce the effective angle of incidence (due to steering towards the surface) as well as the resulting surface roughness.
[18] While the deposition angle and experimental geometry were not precisely controlled in these experiments, a recent estimate for the range of deposition angles is $\theta = 56^o \pm 10^o$ (P. Miceli, private communication).
[19] J.W. Evans, D.E. Sanders, P.A. Thiel, and A.E. DePristo, Phys. Rev. B **41**, R5410 (1990).
[20] M.W. Finnis and V. Heine, J. Phys. F: Metal Phys. **4**, L37 (1974).